Taylor & Francis
Taylor & Francis Group

RESEARCH ARTICLE

Biodegradable hollow mesoporous organosilica nanotheranostics (HMONs) as a versatile platform for multimodal imaging and phototherapeutic-triggered endolysosomal disruption in ovarian cancer

Pengfei Li[a]*, Bingquan Lin[b]*, Zhian Chen[c]*, Pan Liu[a]*, Jiaqi Liu[a], Weili Li[a], Ping Liu[a], Zhaoze Guo[d] and Chunlin Chen[a]

[a]Department of Obstetrics and Gynecology, Nanfang Hospital, Southern Medical University, Guangzhou, China; [b]Department of Medical Imaging Center, Nanfang Hospital, Southern Medical University, Guangzhou, China; [c]First Clinical Medical College, Southern Medical University, Guangzhou, China; [d]Breast Center, Department of General Surgery, Nanfang Hospital, Southern Medical University, Guangzhou, China

ABSTRACT

A major impediment in the development of nanoplatform-based ovarian cancer therapy is endo/lysosome entrapment. To solve this dilemma, a hollow mesoporous organosilica-based nanoplatform (HMON@CuS/Gd$_2$O$_3$) with a mild-temperature photothermal therapeutic effect and multimodal imaging abilities was successfully synthesized. HMON@CuS/Gd$_2$O$_3$ exhibited an appropriate size distribution, L-glutathione (GSH)-responsive degradable properties, and high singlet oxygen generation characteristics. In this study, the nanoplatform specifically entered SKOV-3 cells and was entrapped in endo/lysosomes. With a mild near infrared (NIR) power density (.5 W/cm^2), the HMON@CuS/Gd$_2$O$_3$ nanoplatform caused lysosome vacuolation, disrupted the lysosomal membrane integrity, and exerted antitumour effects in ovarian cancer. Additionally, our in vivo experiments indicated that HMON@CuS/Gd$_2$O$_3$ has enhanced T1 MR imaging, fluorescence (FL) imaging (wrapping fluorescent agent), and infrared thermal (IRT) imaging capacities. Using FL/MRI/IRT imaging, HMON@CuS/Gd$_2$O$_3$ selectively caused mild phototherapy in the cancer region, efficiently inhibiting the growth of ovarian cancer without systemic toxicity in vivo. Taken together, the results showed that these well-synthesized nanoplatforms are likely promising anticancer agents to treat ovarian cancer and show great potential for biomedical applications.

Introduction

The incidence rate of ovarian cancer ranks third among female reproductive system malignant tumors, but the mortality rate ranks first (Bray et al., 2018; Sung et al., 2021). Because the clinical symptoms of early-stage ovarian cancer are atypical and lack specificity, early-stage tumors are challenging to detect, and 70% of ovarian cancers are diagnosed as stage III or IV. Ovarian cancer is also associated with a poor prognosis; approximately 70% of patients have a survival time of less than five years, and approximately 70% of patients have tumors that relapse within three years after surgery (Jayson et al., 2014; Lheureux et al., 2019). Therefore, novel strategies for diagnosis and treatment are needed to improve the survival of patients with ovarian cancer.

The lysosome is a crucial organelle – the digestive organ in cells (Zhu et al., 2017; Nakamura et al., 2019). Because of their strong degradation ability, lysosomes can remove cytotoxic substances, damaged or dead organelles, and mismatched proteins to maintain intracellular homeostasis (Mukherjee et al., 2019). Lysosomes also regulate intracellular signal transduction pathways. When the tumor microenvironment is hypoxic and undernourished, an alternative energy source is rapidly provided by degrading and recycling cellular components through lysosomes to meet the needs of cell growth and proliferation (Zhu et al., 2021). Therefore, tumor development and progression are closely related to the function of lysosomes, and triggering lysosome damage may be an effective method to induce tumor cell death.

Nanomedicines have recently been widely used in cancer therapy (Chen et al., 2021; Guo et al., 2021). Most nanoparticles (NPs) will be phagocytized into lysosomes after entering tumor cells through the endosomal pathway (Guo et al., 2018; Jin et al., 2021). Therefore, many scholars have

developed NPs with 'lysosomal escape' to improve the concentration of drugs in the cytoplasm (Zhang et al., 2018, 2020). Additionally, several studies have validated that photosensitive NPs are an effective way to destroy the lysosome membrane induced by near infrared (NIR) irradiation, promoting NPs to escape from lysosomes and then playing an effective therapeutic role in the cytoplasm (Jiang et al., 2020; Shi et al., 2020). Therefore, we developed smart NPs that could directly damage lysosomes under NIR irradiation to achieve good antitumour effects.

NIR-based phototherapy (PT) has attracted more attention for the targeted treatment of malignant tumors because of the advantages of minimal harm to normal tissues, noninvasiveness, and efficient therapeutic ability. The combination of mild photothermal therapy (PTT) and photodynamic therapy (PDT) can achieve much better therapeutic efficiency because mild hyperthermia can elevate the level of oxygen in the tumor because of the temperature increase in blood flow, thus overcoming hypoxia associated resistance to PDT (Yu et al., 2021). Several Cu-based nanoparticles have shown good photothermal conversion efficiency and unique photodynamic capability under NIR laser light illumination (Li et al., 2018; Tang et al., 2020). Among them, mesoporous silica nanoparticles (MSNs) and porous hollow silica nanoparticles have been studied as drug delivery systems because of their good *in vitro* and *in vivo* biocompatibility (Jiang et al., 2021). Recently, the incorporation of disulfide bonds (–S–S–) into the silica framework has helped to achieve fast degradation of organic/inorganic hybrid nanoparticles through intracellular glutathione (GSH) stimulation (Li et al., 2020; Wu et al., 2021). For example, Chen et al. (2020) reported a structure-dependent, GSH-responsive biodegradable, dendritic mesoporous organosilica nanoparticle that performed as an efficient delivery platform for therapeutic biomacromolecules in cancer treatment. Shi et al. identified an organic–inorganic hybridized hollow mesoporous organosilica nanoparticle (HMON) based on a 'chemical homology' mechanism for guest drug molecule encapsulations (Huang et al., 2017). Inspired by these studies, HMONs with a disulfide-bonded hybrid framework were selected as a model drug delivery system in our study. Different from other methods, CuS nanocrystals were grown *in situ* onto the surface of HMONs without the help of thiol groups, and HMON@CuS NPs were synthesized (Guo et al., 2020); these HMON@CuS NPs exhibited good photothermal conversion efficiency and better biocompatibility. However, the role of HMON@CuS NP-produced PTT&PDT in inducing lysosome damage in ovarian cancer remains unclear.

Furthermore, identifying and eliminating visible tumors is the main method to improve the prognosis and reduce the recurrence rate of ovarian cancer patients. However, completely removing the lesions in traditional surgery is challenging, particularly in patients with extensive peritoneal metastasis. NIR-based PTT and PDT are potential methods to eliminate microinvasive lesions. Using fluorescence and MR multimodality imaging, we can achieve real-time visualization of tumor identification and PT and identify an effective time window for PT intervention.

Herein, we attempted a novel theranostic nanoplatform by integrating DIR and Gd_2O_3 into HMON@CuS NPs to form the versatile platform HMON@CuS/Gd_2O_3 for MRI/NIR fluorescence multimodality imaging-guided PT. HMONs served as nanocarriers, CuS served as a photothermal agent, Gd_2O_3 served as an MRI contrast enhancer, and DIR served as an NIR fluorescence imaging agent. Therefore, HMON@CuS/Gd_2O_3 NPs can generate local hyperthermia and oxidative stress elevation at tumor lesions and achieve real-time visualization of tumor identification and elimination. After treatment with HMON@CuS/Gd_2O_3 under NIR irradiation, the *in vitro* and *in vivo* ovarian cancer proliferation abilities were evaluated. Additionally, lysosomal disruption was detected to explain the antitumour mechanism induced by HMON@CuS/Gd_2O_3. Thus, the multifunctional nanoplatform HMON@CuS/Gd_2O_3 might present great potential for precise cancer theranostics in ovarian cancer.

Materials and methods

Materials

Cetyltrimethylammonium chloride solution (CTAC), triethanolamine (TEA), tetraethoxysilane (TEOS), sodium citrate (3-mercaptopropyl)-trimethoxysilane (MPTES), concentrated HCl (37%), $NH_3•H_2O$, $Na_2S•9H_2O$, $CuCl_2•2H_2O$, $Gd_2Cl_3•6H_2O$, 25 wt% bis [3-(triethoxysilyl)propyl]tetrasulfide (BTES), and NaOH were purchased from Sigma–Aldrich (MO, USA). The C18PMH-mPEG was purchased from Laysan Bio Inc. (AL, USA). PBS, DMEM, fetal bovine serum (FBS), and .05% trypsin-EDTA were obtained from Gibco (NY, USA). Human ovarian cancer cells (SKOV-3) were purchased from the cell bank of the Chinese Academy of Sciences (Shanghai, China).

Synthesis of HMON

According to a previous study, we performed an ammonia-assisted selective etching strategy to construct the hollow structure of HMON nanocarriers. Briefly, 20 mL of deionized water (ddH_2O) was mixed with 2.1 mL of CTAC and 50 μl of TEA solution and stirred at 95 °C, and then 1 mL of TEOS was added dropwise to the mixed solution. One hour later, a mixture of BTES (1 mL) and TEOS (1 mL) was added dropwise and reacted for another 4 h. After that, the mixture was collected and washed with absolute ethanol, followed by stirring with HCl solution at 80 °C for 12 h. The mixture was further etched with ammonia solution at 60 °C for 3 h; finally, the HMON products were obtained after centrifugation.

Synthesis of HMON@CuS@Gd_2O_3

First, 30 mg of HMON products was stirred with 15 mg of $CuCl_2·6H_2O$ in aqueous solutions. Six hours later, 30 mg of Na_2S was added and stirred overnight at room temperature. After centrifugation and washing with ddH_2O, the HMON@CuS NPs were collected and stored at 4 °C. To synthesize ultrasmall gadolinium oxide nanoparticles (Gd_2O_3), we first added 600 mg of gadolinium chloride hexahydrate into 10 mL of diethylene glycol (DEG). Subsequently, the

mixture solution was vigorously stirred (750 rpm) at 80 °C. One hour later, 1.125 mL of aqueous NaOH solution (1 mmol/L) was added and stirred at 140 °C for 1 h, followed by stirring at 180 °C for 4 h; finally, ultrasmall Gd_2O_3 nanoparticles were obtained. After that, 5 mL of as-prepared Gd_2O_3 solution and 2 mL of as-prepared HMON@CuS solution (50 mg/mL) were mixed and sonicated at room temperature for 24 h. Finally, the products (HMON@CuS/Gd_2O_3) were obtained by centrifugation and washed with water several times.

Characterization of HMON@CuS/Gd_2O_3

The morphology of HMON@CuS/Gd_2O_3 was investigated using a transmission electron microscope (Jeol JEM-2000F, Tokyo, Japan). The particle size, size distribution, and zeta potential of the nanoparticles were measured using the dynamic light scattering assay (Zetasizer Nano ZS, Malvern, UK). The UV-visible absorption spectrum of HMON@CuS/Gd_2O_3 was measured using a spectrometer (Shimadzu UV-2600 UV, Kyoto, Japan). The morphologies of the PIH and PIGH NPs were examined using scanning electron microscopy (SEM; JEOL JSM-6301F, Tokyo, Japan). X-ray photoelectron spectroscopy (XPS) was performed using a PHI 5000 VersaProbe spectrometer and a monochromatic AlKα radiation source. Various concentrations of HMON@CuS/Gd_2O_3 in PBS solutions were irradiated using an 808 nm NIR laser (FS-Optics, Changchun, China), and the real-time temperatures were recorded using infrared thermography (FLIR E50 camera system, Shanghai, China).

The pH calculation of the photothermal conversion efficiency

Photothermal conversion efficiency of HMON@CuS/Gd_2O_3 was determined according to previous method. Detailed calculation was given as following:

$$\eta = \frac{hS(T_{max} - T_{max,water}) - Q_{dis}}{I(1 - 10^{-A_{808}})} \times 100\% \tag{S1}$$

$$Q_{dis} = \frac{C_D M_D (T_{max(water)} - T_{amb})}{\tau_{S(water)}} \tag{S2}$$

$$\theta = \frac{t - T_{amb}}{T_{max} - T_{amb}} \tag{S3}$$

$$t = -\tau_S \times \ln \theta \tag{S4}$$

$$\tau_S = \frac{C_D M_D}{hS} \tag{S5}$$

The photothermal conversion efficiency, η, is calculated using Equation (S1). The T_{max} means the equilibrium temperature, T_{amb} is ambient temperature of the surroundings. The Q_{dis} is heat loss from light absorbed by the container, and it is calculated by Equation (S2). I represents the incident laser power, 'A808' is the absorbance of samples at 808 nm. Where h means heat transfer coefficient, S represents the surface area of the container, and the hS is calculated from the Figure S(2B). The hS is calculated using the following Equation (S5).

In vitro MR imaging

T1-weighted MR imaging of HMON@CuS/Gd_2O_3 (Gd^{3+} concentrations from .025 to .4 mM) was performed using a 3.0 T MRI scanner (Philips Ingenia 3.0 T, The Netherlands). The longitudinal proton relaxation times (T1) of HMON@CuS/Gd_2O_3 were measured using T1-weighted maps to calculate the relaxation rate.

Evaluation of the photothermal efficiency of HMON@CuS/Gd_2O_3

HMON@CuS/Gd_2O_3 solutions of 30, 60, 80, and 100 µg/mL were irradiated with an 808-nm NIR laser (FS-Optics, Changchun, China) at a power of .5 W/cm^2 for 5 min. Blank PBS was used as a negative control. The temperature was recorded by infrared thermography (FLIR E50 Camera System, Shanghai, China). Additionally, the HMON@CuS/Gd_2O_3 solution of 80 µg/mL was irradiated with an 808 nm NIR laser (FS-Optics, Changchun, China) at a power of 1.0 W/cm^2, .5 W/cm^2, and .3 W/cm^2 for 5 min, respectively.

Cell uptake of HMON@CuS/Gd_2O_3

SKOV-3 cells were seeded on 12-well plates (2×10^5 cells/well) and cultured in DMEM containing 10% FBS and 1% penicillin-streptomycin solution (Gibco) in a humidified incubator (5% CO_2 at 37 °C) for 24 h. The cells were then incubated with HMON@CuS/Gd_2O_3-containing medium (50 µg/mL) for 6 h and 24 h. Subsequently, the cells were observed by TEM and CLSM images to analyze the cellular uptake of HMON@CuS@Gd_2O_3.

In vitro phototherapeutic effect of HMON@CuS/Gd_2O_3

SKOV-3 cells were seeded on 96-well culture plates (6000 cells/well) and incubated in DMEM containing 10% FBS and 1% penicillin-streptomycin solution (Gibco) for 24 h. The cells were then incubated with fresh medium containing various concentrations of HMON@CuS/Gd_2O_3 for 6 h. Subsequently, the cells were washed twice with PBS and then irradiated at 808 nm at a power density of .5 W/cm^2 for 5 min or without irradiation. After 24 h of incubation, cell viability was assessed using a standard Cell Counting Kit-8 (CCK-8) and LDH Assay Kit.

Intracellular distribution

SKOV-3 cells were seeded in 20 mm glass-bottomed dishes and incubated with HMON@CuS/Gd_2O_3-containing medium (50 µg/mL) for 0 h, 6 h, 12 h, and 24 h. Subsequently, the cells were washed with cold PBS and stained with LysoTracker Green DND-26 for 15 min and Hoechst 33342 for 10 min to label lysosomes and nuclei, respectively. Finally, the cells were washed with cold PBS and observed with CLSM. The morphology of lysosomes was observed in cells incubated with saline-containing medium or HMON@CuS/Gd_2O_3-containing medium with or without NIR irradiation for 5 min (808 nm, .5 W/cm^2) using a similar procedure.

The morphology of lysosomes was also observed by TME. Briefly, SKOV-3 cells were seeded on six-well plates (4×10^5 cells/well) and cultured in DMEM containing 10% FBS and 1% penicillin–streptomycin solution (Gibco) in a humidified incubator (5% CO_2 at 37 °C) for 24 h. The cells were then incubated with HMON@CuS/Gd_2O_3-containing medium (50 μg/mL) for 6 h and treated with NIR irradiation for 5 min (808 nm; .5 W/cm²). The cells incubated with saline-containing medium and treated with NIR irradiation served as the blank control group. Finally, the cell samples were made into ultrathin sections, and the morphology of lysosomes was observed by TEM.

Measurement of intracellular ROS level
Briefly, cells were seeded in 24-well plates, and 24 h later, were HMON@CuS/Gd_2O_3 NPs added. The plates were subsequently treated with or without NIR irradiation. The cells were washed with PBS 24 h later and then sequentially stained with DCFH-DA reagent for 20 min, before imaging by fluorescence microscopy.

Integrity of the lysosomal membrane
Cells were plated in 24-well plates and cultured overnight. Twenty-four hours later, HMON@CuS/Gd_2O_3 NPs were introduced into SKOV-3 cells and cultured overnight. After PBS rinsing, the cells were treated with AO (5 μg mL^{-1}) for 15 min and then rinsed with PBS. Next, the cells were observed under a fluorescence microscope, and the samples were excited at 488 nm. Emission was detected at 537 nm (green) and 615 nm (red).

In vivo multimodal imaging behaviors of HMON@CuS/Gd_2O_3
All animal experiments were conducted in accordance with the guidelines of the Institutional Animal Care and Use Committee (IACUC). The female nude mouse tumor model was constructed by the subcutaneous injection of SKOV-3 cells (2×10^6 cells/mouse). When the tumor volumes reached 50–100 mm³, HMON@CuS/Gd_2O_3 NP solution was intravenously injected into the tumor-bearing mice. In vivo fluorescence imaging of tumor-bearing mice was conducted using a white-light and near-infrared dual-channel image-guided device (DIGITAL PRECISION MEDICINE Company, Beijing, China) at 6, 12, and 24 h after injection. For ex vivo fluorescence imaging, the tumor-bearing mice were sacrificed at 24 h, and the excised heart, liver, spleen, lung, kidney, brain, and tumor tissues were evaluated.

For in vivo MR imaging, SKOV-3 tumor-bearing mice were intravenously injected with HMON@CuS/Gd_2O_3 NP solution. T1-weighted MR images of the tumor area before and 24 h postinjection were collected using a 3.0 T Philips Ingenia MRI scanner with a special animal coil.

To perform in vivo IRT imaging, SKOV-3 tumor-bearing mice were also injected with HMON@CuS/Gd_2O_3 NP solution. Subsequently, the mice were irradiated with 808 nm irradiation at .5 W/cm² for 8 min before and 24 h post-injection. The minimal tumor temperature changes during laser irradiation were monitored using an IR thermographic camera.

In vivo phototherapeutic effect of HMON@CuS/Gd_2O_3
SKOV-3 cells were collected and inoculated subcutaneously into the flanks of the right hind leg of mice. When the tumor size reached 50–100 mm³, various formulations were applied, such as saline with or without NIR, HMON@CuS/Gd_2O_3 with or without NIR irradiation (four mice/group), followed by 5 min of irradiation at the tumors (808 nm; .5 W/cm²) at 24 h post-injection. The length and width of the tumors were measured using a caliper. The corresponding tumor volume was calculated using the following formula: tumor volume (V) = length × width²/2. Finally, the mice were sacrificed, and the tumors were isolated to evaluate the therapeutic efficacy of different groups. The body weight of the mice was also monitored during treatments.

Statistical analysis
Metrological data were presented as means ± standard deviation ($n \geq 3$). To compare two groups of data, Student's t-test (two-tailed) was used. To compare more than two groups of data, analysis of variance (ANOVA), followed by multiple comparisons of Tukey's test was used. The statistical software used was SPSS 23.0 (SPSS, Inc., Chicago, IL, USA). $p < .05$ was considered statistically significant.

Results and discussion
Preparation and characterization of HMON@CuS/Gd_2O_3
HMON@CuS/Gd_2O_3 nanoparticles with uniform sizes of approximately 70 nm were synthesized (Figure 1(A)). Additionally, elemental mapping revealed that Si, Cu and Gd elements were distributed on the surface of these nanocomposites, but their contents in the central area were low, indicating that the nanocomposites had hollow structures (Figure 1(B)). DLS revealed that the diameter of HMONs was 74.53 ± 2.11 nm, while CuS and/or Gd_2O_3 loading led to a slight increase in the size of HMON@CuS (77.09 ± 1.39 nm) and HMON@CuS/Gd_2O_3 (78.45 ± 1.02 nm), and all of them exhibited a unimodal size distribution (Figure 1(C)). Additionally, the zeta potentials of HMON, HMON@CuS and HMON@CuS/Gd_2O_3 were approximately $-28 \pm .84$ mV, $-19 \pm .93$ mV and $-15 \pm .67$ mV, respectively (Figure 1(C)). The mass ratio of Cu and Gd content in HMON@CuS/Gd_2O_3, as determined by inductively coupled plasma-atomic emission spectroscopy (ICP-AES), were almost 3:1. The FT-IR results revealed that HMON@CuS/Gd_2O_3 showed strong and broad peaks at 2926.62 cm^{-1} and 2955.43 cm^{-1} (attributed to -CH_2 of C18PMH-mPEG chains) (Liu et al., 2020), characteristic peaks at 1103.05 cm^{-1} and 470.40 cm^{-1} (attributed to -Si-O- of HMON), and a characteristic peak at 689.55 cm^{-1} (attributed to –Cu–S–) (He et al., 2018) (Figure 1(D)). The XPS results (Park et al., 2018) demonstrated that the HMON@CuS/Gd_2O_3 NPs possessed C (C 1s peaks at 284.73 eV), O (O 1s peaks at 532.23 eV), Si (Si 2p peaks at 102.58 eV), Cu (Cu 2p peaks at 932.68 eV), S (S 2p peaks at 169.88 eV) and Gd (Gd 4d peaks at 143.48 eV; Gd 3d peaks at 1187.98 eV and 1220.88 eV) (Figure 1(E)). Finally, the XRD results demonstrated the presence of a typical covellite crystalline phase of
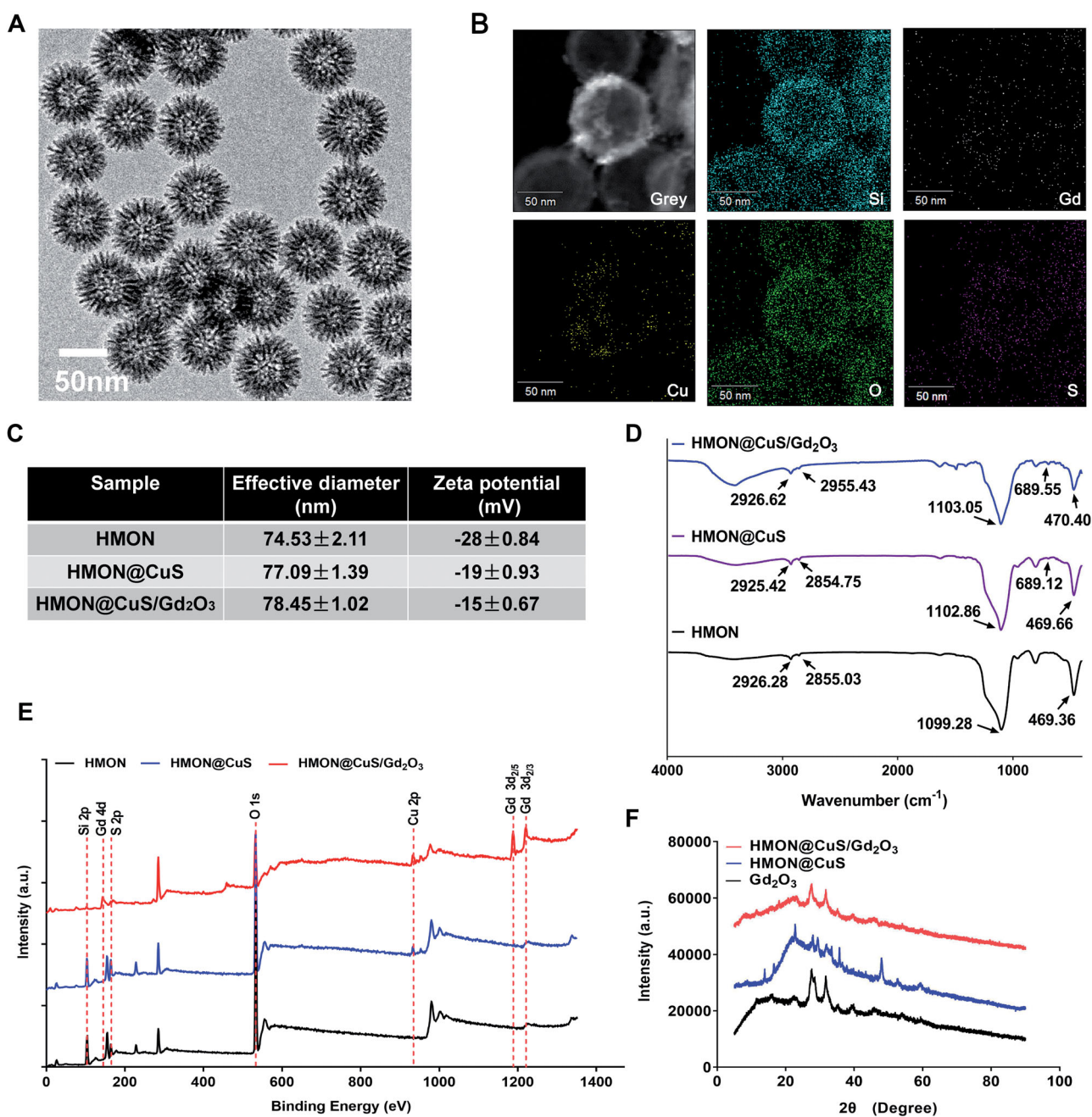
Figure 1. Characterization of HMON@CuS/Gd$_2$O$_3$. (A) Transmission electron microscopy (TEM) images of HMON@CuS/Gd$_2$O$_3$. Scale bar, 50 nm. (B) Element mapping images of HMON@CuS/Gd$_2$O$_3$. Scale bar, 50 nm. (C) Size distribution and zeta potential of HMON@CuS/Gd$_2$O$_3$ nanoparticles characterized by DLS. (D) Fourier transform infrared (FT-IR) spectra of HMON@CuS and HMON@CuS/Gd$_2$O$_3$ NPs. (E) X-ray photoelectron spectroscopy (XPS) of HMON and HMON@CuS/Gd$_2$O$_3$ NPs. (F) X-ray diffraction (XRD) patterns of HMON and HMON@CuS/Gd$_2$O$_3$ NPs.

CuS and Gd$_2$O$_3$ on the HMON surface (Figure 1(F)). Taken together, these results consistently suggested the successful synthesis of HMON@CuS/Gd$_2$O$_3$.

Photothermal efficiency of HMON@CuS/Gd$_2$O$_3$

Because of the presence of disulfide bonds in the skeleton of HMONs, HMON@CuS/Gd$_2$O$_3$ NPs can be biodegraded in response to the high concentration of GSH (Hadipour Moghaddam et al., 2018; Li et al., 2020). TEM images revealed that when exposed to 10 mM GSH solution for 14 days, the completely hollow nanoparticles were hardly visible (Figure 2(A)). Similarly, the HMON@CuS/Gd$_2$O$_3$ were immersed into different concentration of GSH solution (0, 5, and 10 mM), respectively, and the degradation process was also monitored by ICP tests. As shown in the Figure S1, the Si ions release percentage reached approximately 28.2% dissolved in GSH solution (GSH = 10 mM), whereas only 15.9% was released in the absence of GSH after 60 h. Additionally, because of the presence of Gd$_2$O$_3$ (Zohdiaghdam et al., 2013; Fang et al., 2014), the as-prepared NPs were expected to be a promising MRI imaging contrast agent, a finding that was confirmed by *in vitro* MRI scanning (Figure 2(B)). UV–vis spectra results revealed that HMON@CuS and HMON@CuS/Gd$_2$O$_3$ both showed strong absorption in the NIR region, primarily attributed to the CuS nanocrystals (Figure 2(C)).
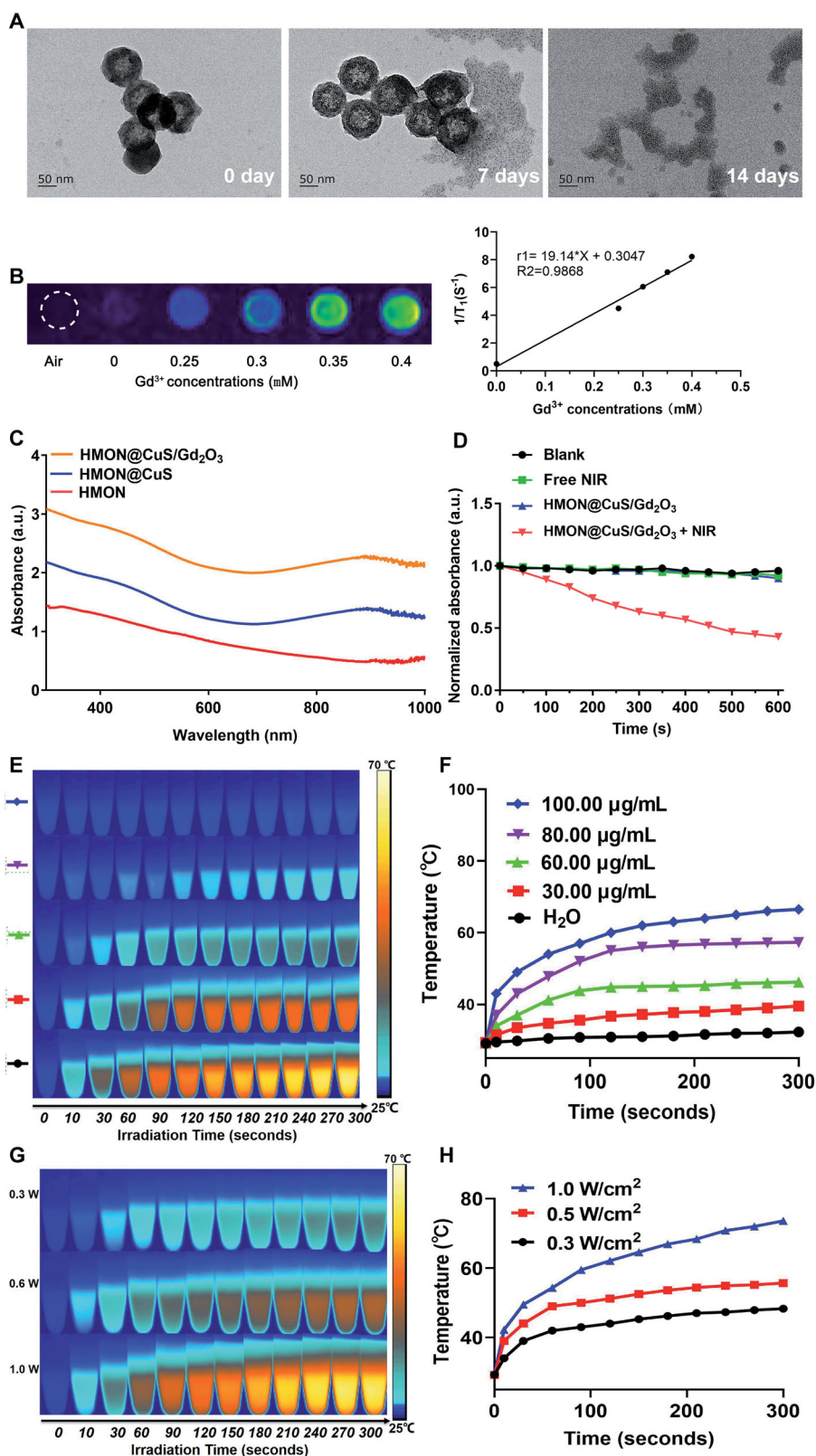
Figure 2. (A) TEM images of biodegradable HMON@CuS/Gd$_2$O$_3$ immersed in 10 mM GSH aqueous solution for 7 days and 14 days. (B) T1-weighted MRI images of HMON@CuS/Gd$_2$O$_3$ at various concentrations. (C) Ultraviolet Visible Spectroscopy (UV-Vis) spectrum. (D) Reactive oxygen species (ROS) production of HMON@CuS/Gd$_2$O$_3$ under NIR irradiation (.5 W/cm^2; 5 min). (E&F) Temperature increase curve induced by different concentrations of HMON@CuS/Gd$_2$O$_3$ aqueous solution under NIR irradiation (1.0 W/cm^2; 5 min). (G&H) Temperature increase curve induced by different NIR power intensities (.3 W/cm^2, .5 W/cm^2, and 1.0 W/cm^2).

Furthermore, the DPBF results revealed that HMON@CuS/Gd$_2$O$_3$ NPs plus NIR irradiation showed lower DPBF absorption, indicating that HMON@CuS/Gd$_2$O$_3$ had a strong photodynamic effect (Figure 2(D)). After NIR laser irradiation (.5 W/cm^2) for 5 min, a dramatic temperature increase was observed in the HMON@CuS/Gd$_2$O$_3$ group, while no obvious temperature change was shown in the PBS group. The maximum increased temperature (ΔT_{max}) of the HMON@CuS/
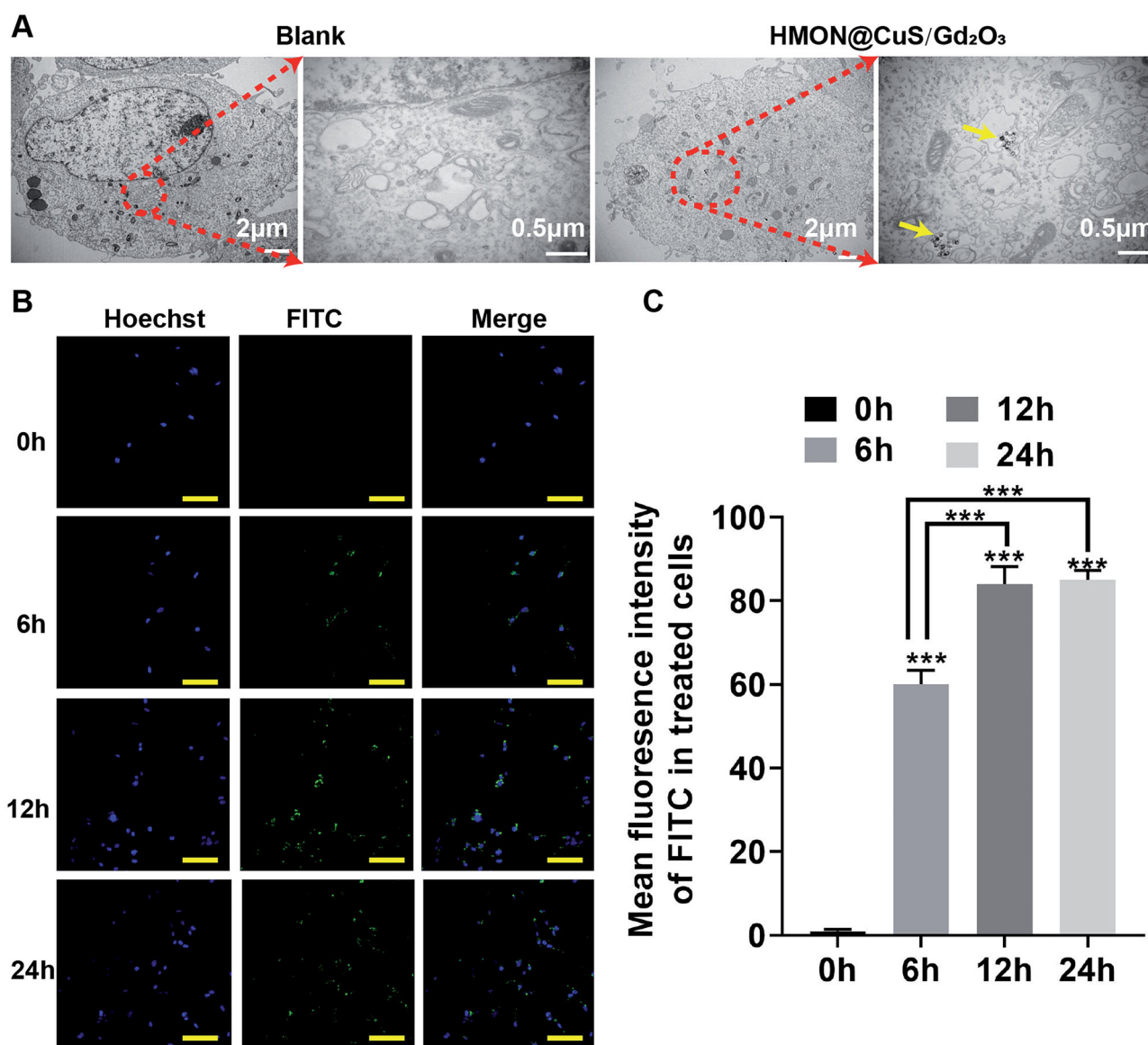
Figure 3. *In vitro* intracellular uptake detection. (A) TEM image of SKOV-3 cells; yellow arrows indicate nanoparticle locations. (B) CLSM images and fluorescence intensity profile analysis of SKOV-3 cells after treatment with FITC-labelled HMON@CuS/Gd$_2$O$_3$. Scale bar, 100 μm. *** $p < .001$.

Gd$_2$O$_3$ group (100 μg/mL) $\sim$37.5 °C, whereas the ΔT_{max} of the other HMON@CuS/Gd$_2$O$_3$ groups (80 μg/mL, 60 μg/mL, and 30 μg/mL) increased to $\sim$29.9 °C, $\sim$17.0 °C, and $\sim$10.2 °C, respectively (Figure 2(E,F)). Furthermore, as the power density of NIR laser irradiation increased from .3 W/cm^2 to 1.0 W/cm^2, the maximum increased temperature (ΔT_{max}) of HMON@CuS/Gd$_2$O$_3$ (80 μg/mL) increased from $\sim$19.0 °C to $\sim$44.2 °C (Figure 2(G,H)). Additionally, according to the linear regression curve between the cooling stage and negative natural logarithm of the driving force temperature of HMON@CuS/Gd$_2$O$_3$, its photothermal conversion efficiency was 34.2% (Figure S2). In total, these results demonstrated that HMON@CuS/Gd$_2$O$_3$ serves as a promising PTT, PDT, and functional MR imaging nanoparticle.

In vitro *cellular uptake*
FITC was encapsulated into HMON@CuS/Gd$_2$O$_3$, and the cellular uptake of HMON@CuS/Gd$_2$O$_3$ was then observed by transmission electron microscopy (TEM) and confocal laser scanning microscopy (CLSM). After incubation with HMON@CuS/Gd$_2$O$_3$ (50 μg/mL) for 6 h, TEM images showed hollow mesoporous nanotheranostics in the cytoplasm of SKOV-3 cells; however, this structure could not be found in the control group (Figure 3(A)). Consistently, the CLSM results indicated that the intracellular FITC fluorescence signal increases with increasing incubation time (Figure 3(B,C)). These obtained results revealed that HMON@CuS/Gd$_2$O$_3$ is internalized into SKOV-3 cells, supporting that NPs exert phototherapeutic and antitumour effects.

In vitro *phototherapeutic effect of HMON@CuS/Gd$_2$O$_3$*
The *in vitro* phototherapeutic effects of HMON@CuS/Gd$_2$O$_3$ in the dark or under NIR irradiation were investigated in SKOV-3 cells based on the CCK-8 assay. First, SKOV-3 cells were incubated with HMON@CuS/Gd$_2$O$_3$ at different concentrations for 6 h and then were irradiated with an 808 nm
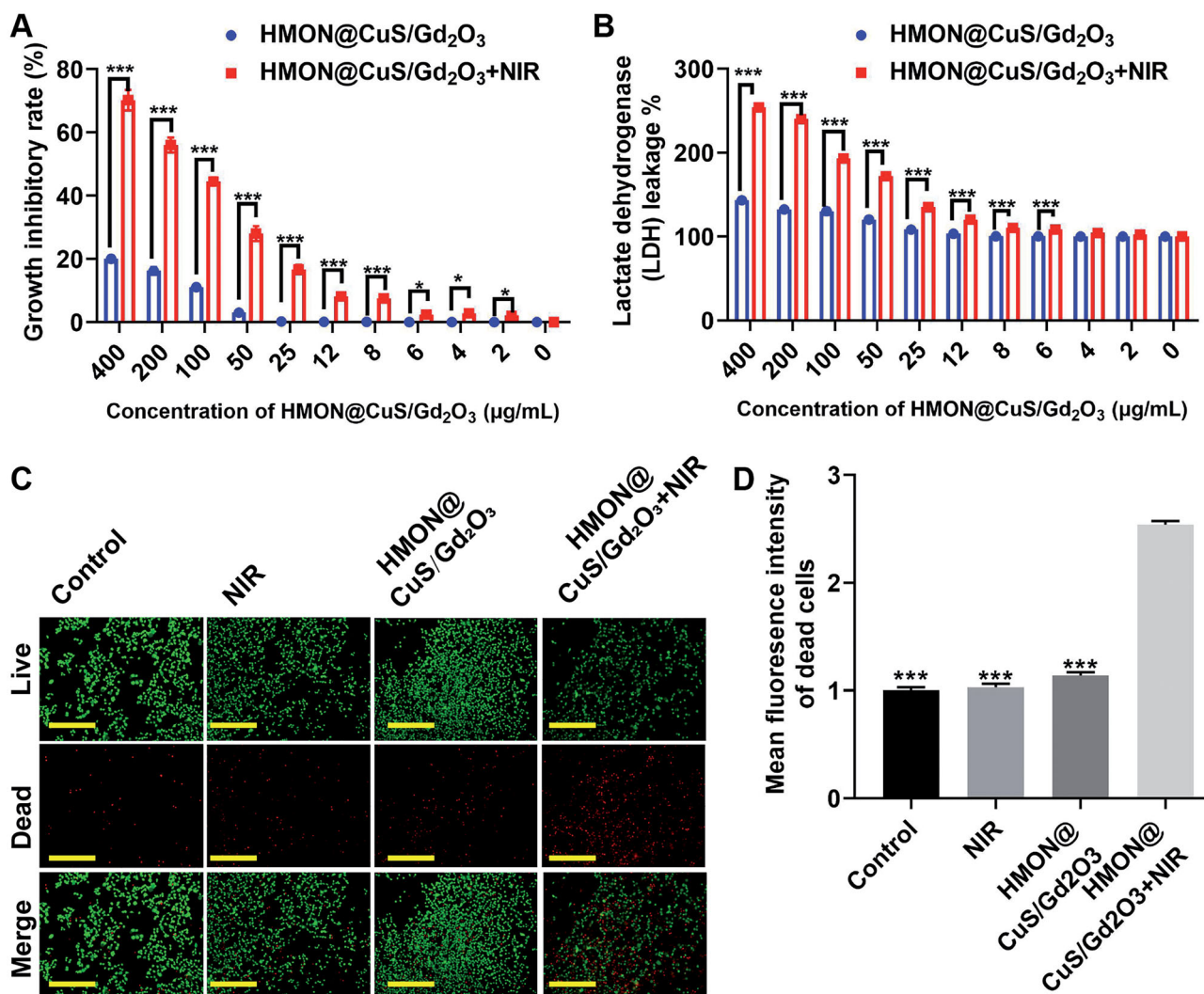
Figure 4. *In vitro* antitumour effect after treatment with HMON@CuS/Gd$_2$O$_3$ NPs. (A) Growth inhibitory rate of SKOV-3 cells detected by the CCK-8 assay. (B) LDH leakage of SKOV-3 cells after treatment with HMON@CuS/Gd$_2$O$_3$ plus NIR. (C&D) Live/dead assay and relative statistical analysis for SKOV-3 cells treated with HMON@CuS/Gd$_2$O$_3$ NPs with or without NIR irradiation (.5 W/cm^2; 5 min) (Green: Live cells; Red: Dead cells). Scale bar, 150 μm. $^*p < .05$, $^{***}p < .001$.

laser at a power density of .5 W/cm^2 for 5 min. Next, the antitumour therapeutic efficacies of NPs were tested using the CCK-8 assay after 24 h. The CCK-8 assay revealed that HMON@CuS/Gd$_2$O$_3$ in the dark did not induce significant changes in cell death. In the presence of NIR irradiation, the cell viability was dramatically decreased. At 12, 25, 50, 100, and 200 μg/mL of HMON@CuS/Gd$_2$O$_3$, the cell growth inhibitory rate in the dark was measured as ∼.13%, ∼.26%, ∼3.06%, ∼11.12%, and ∼16.20%, respectively, while the cell growth inhibitory rate under NIR irradiation increased rapidly to ∼8.17%, ∼16.7%, ∼28.05%, ∼44.53%, and ∼56.03%, respectively (Figure 4(A)). These results suggested that HMON@CuS/Gd$_2$O$_3$ provides a promising killing effect to ovarian cancer cells under NIR irradiation.

Consistently, the LDH assay revealed that LDH leakage was maintained at a low level in the dark, even at high HMON@CuS/Gd$_2$O$_3$ concentrations. However, HMON@CuS/Gd$_2$O$_3$ under NIR irradiation induced higher levels of LDH leakage in a concentration-dependent manner (Figure 4(B)). These results suggested that HMON@CuS/Gd$_2$O$_3$ provides promising destruction of the cell membrane structure,

resulting in the release of lactate dehydrogenase from the cytoplasm into the culture medium under NIR irradiation.

Similarly, the abovementioned results were also confirmed by live-dead cell staining. Regarding cell growth, compared with cells in the saline group, saline under NIR irradiation group, and HMON@CuS/Gd$_2$O$_3$ in the dark group, the amounts of red spots (dead cells) significantly increased in HMON@CuS/Gd$_2$O$_3$ in the NIR irradiation group (Figure 4(C,D)). These results demonstrated that HMON@CuS/Gd$_2$O$_3$ can achieve effective therapeutic efficacy under NIR irradiation.

Lysosomal disruption based antitumour effect

Herein, a cell-permeant 2′,7′-dichlorofluorescin diacetate (DCFH-DA) probe was used to measure the intracellular ROS level. As presented in Figure S3, the control group exhibited little fluorescence, even in the presence of NIR irradiation, and negligible fluorescence was also observed in the HMON@CuS/Gd$_2$O$_3$ groups without NIR irradiation. Once exposed to the 808 nm laser irradiation, the HMON@CuS/
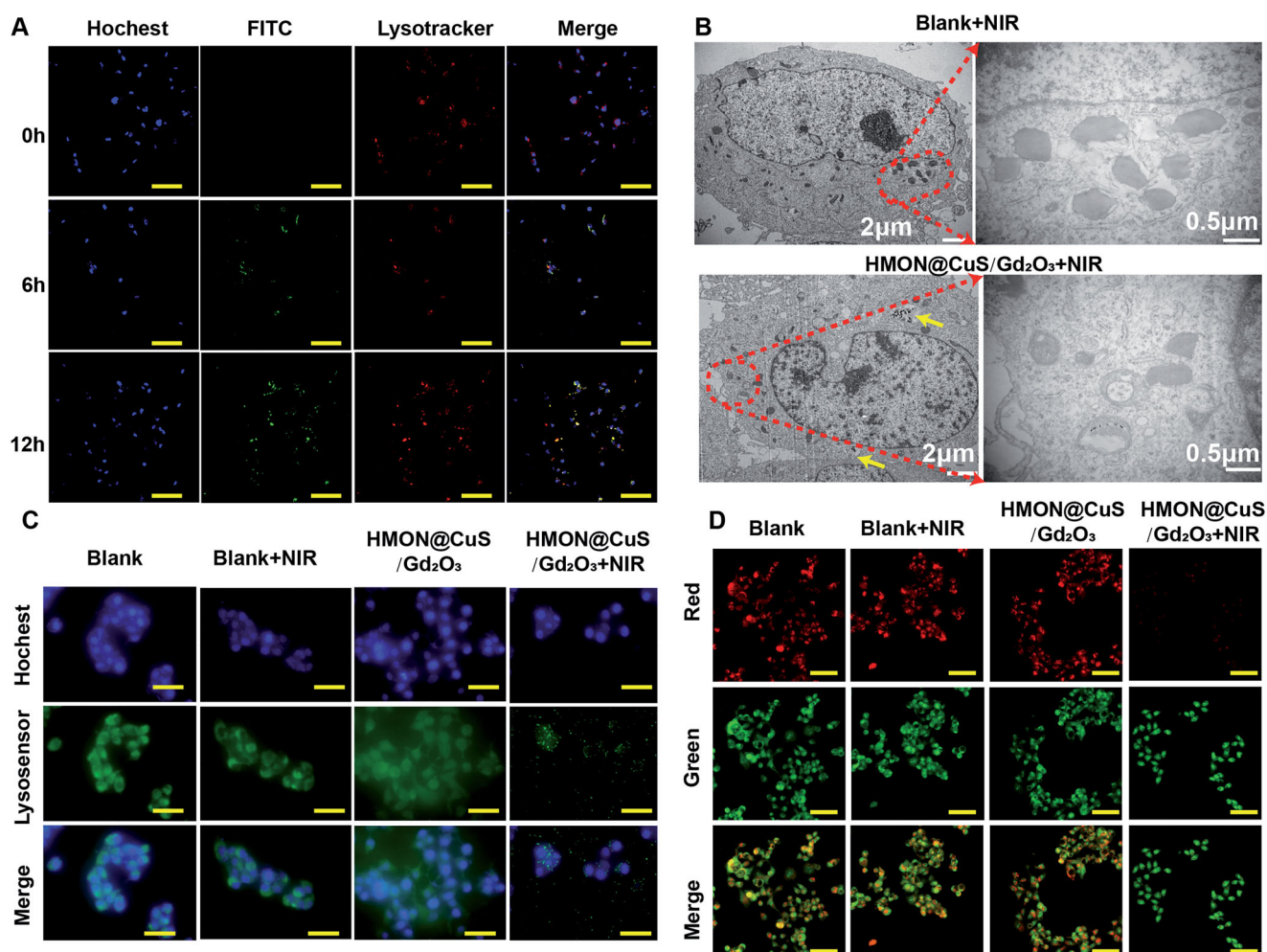
Figure 5. Antitumour mechanism induced by HMON@CuS/Gd$_2$O$_3$ plus NIR based on lysosomal disruption. (A) Confocal imaging of SKOV-3 cells incubated with FITC-labelled HMON@CuS/Gd$_2$O$_3$. At the designated incubation time, the cells were costained with LysoTracker Deep Red and Hoechst 33342 for imaging. Scale bar, 100 μm. (B) TEM images of SKOV-3 cells treated with HMON@CuS/Gd$_2$O$_3$ plus NIR irradiation. (C) Fluorescence images of SKOV-3 cells stained with LysoSensor Green DND-189 (scale bar, 30 μm). (D) Confocal imaging of SKOV-3 cells preincubated with HMON@CuS/Gd$_2$O$_3$ plus NIR irradiation followed by staining with acridine orange (AO). Scale bar, 50 μm.

Gd$_2$O$_3$ group showed higher DCF fluorescence, indicating that HMON@CuS/Gd$_2$O$_3$ could generate ROS and be used for PDT. To further investigate the mechanism of therapeutic efficacy of HMON@CuS/Gd$_2$O$_3$ under NIR irradiation, SKOV-3 cells were incubated with FITC-labelled HMON@CuS/Gd$_2$O$_3$ for 6 and 12 h. Subsequently, cells were stained with LysoTracker (Chen et al., 2012) (a dye specific for lysosomes with red fluorescence emission) and observed by CLSM. Compared with cells in the control group, the green fluorescence of HMON@CuS/Gd$_2$O$_3$ overlapped with the red fluorescence of the lysosome without NIR irradiation, and the yellow spots increased significantly over time (Figure 5(A)), indicating that HMON@CuS/Gd$_2$O$_3$ is located in the lysosome after internalization into SKOV-3 cells. TEM images demonstrated that lysosomes showed differences in shape and size, and lysosome vacuolation was occasionally observed after NIR laser irradiation (Figure 5(B)).

Additionally, after incubation with LysoSensor Green DND-189, the green fluorescence of the lysosome almost disappeared under NIR irradiation relative to the saline group, saline under NIR irradiation group, and HMON@CuS/Gd$_2$O$_3$ in the dark group, indicating that the skeleton structure of the lysosome was almost completely destroyed by HMON@CuS/Gd$_2$O$_3$ under NIR irradiation (Figure 5(C)). Furthermore, in this study, we performed an AO staining assay to evaluate the integrity of the lysosomal membranes (Zhang et al., 2014). Similar to the blank group, the cells treated with HMON@CuS/Gd$_2$O$_3$ showed red fluorescent dots, indicating that the lysosomal membranes were integrated (Figure 5(D)). However, negligible red fluorescent dots were observed in the cells incubated with HMON@CuS/Gd$_2$O$_3$ plus NIR irradiation, demonstrating that the phototherapeutic effect can rupture the lysosomal membrane structure and increase lysosomal membrane permeation. Thus, lysosomal disruption plays a critical role in the antitumour effect of HMON@CuS/Gd$_2$O$_3$.

In vivo *multi-mode imaging of HMON@CuS@Gd$_2$O$_3$*

The fluorescence, MRI, and infrared thermal (IRT) multimodality imaging functionalities of HMON@CuS/Gd$_2$O$_3$ were evaluated in SKOV-3 tumor-bearing mice. Before fluorescence imaging, DIR, a near-infrared carbocyanine dye (Qu et al., 2020), was encapsulated into HMON@CuS/Gd$_2$O$_3$ NPs
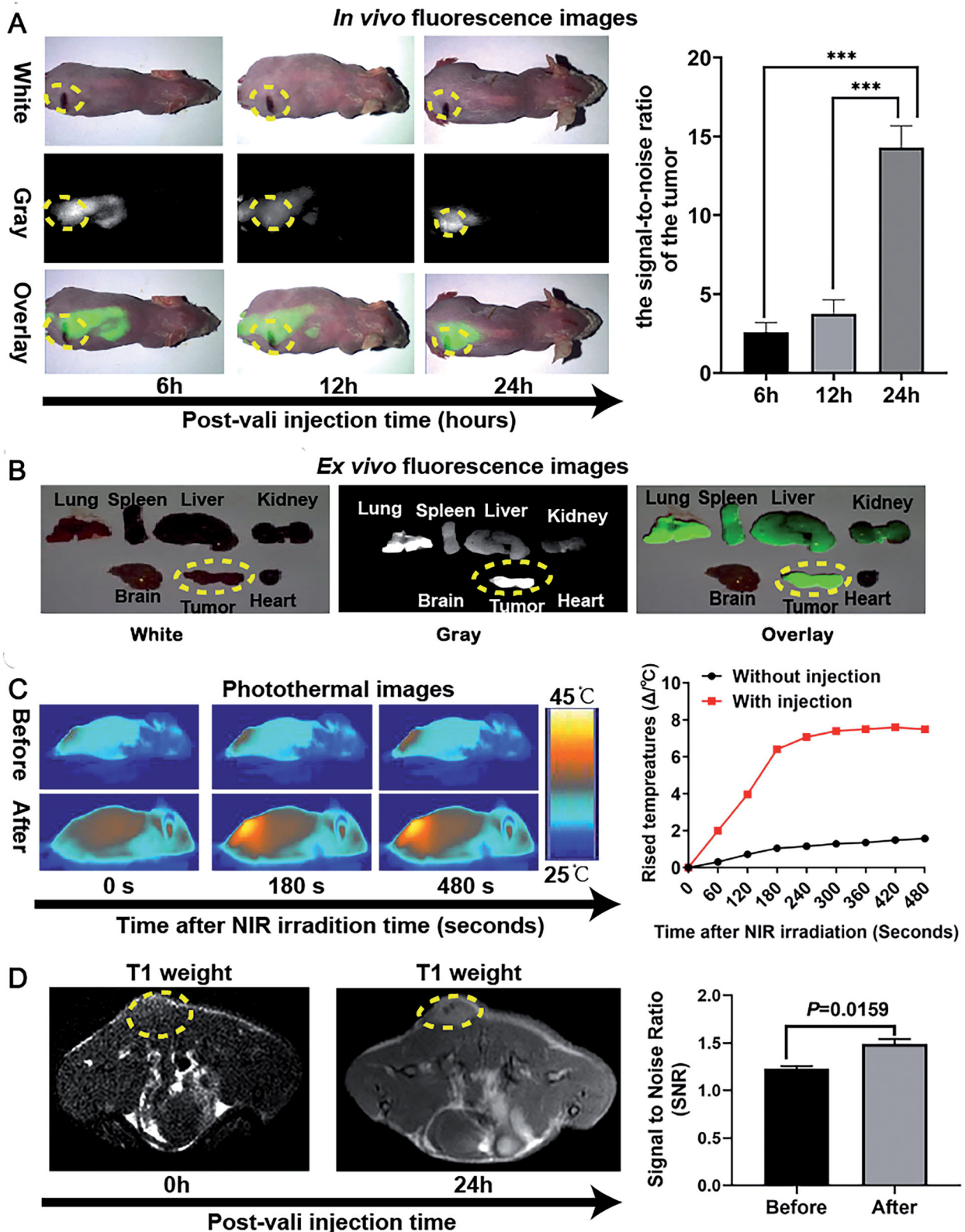
Figure 6. *In vivo* multimode imaging behaviors of HMON@CuS/Gd$_2$O$_3$ NPs in SKOV-3 cells. (A&B) *In vivo* and *ex vivo* fluorescence images of tumor-bearing mice 6, 12, and 24 h after treatment with HMON@CuS/Gd$_2$O$_3$ NPs, *** $p < .001$. (C) IRT images (left) and statistical temperature changes (right) of tumor-bearing mice at the indicated time points. (D) MRI images (left) and statistical signal-to-noise ratio (right) of tumor-bearing mice.

(HMON@CuS/@Gd$_2$O$_3$-DIR). Fluorescence images were acquired using a white-light and near-infrared dual-channel image-guided device (DIGITAL PRECISION MEDICINE Company, Beijing, China). Fluorescence signals were observed at the tumor site 6, 12, and 24 h after injecting HMON@CuS/Gd$_2$O$_3$ NPs intravenously into tumor-bearing mice, with maximal fluorescence intensity after 24 h (Figure 6(A)). Twenty-four hours later, the excised heart, liver, spleen,
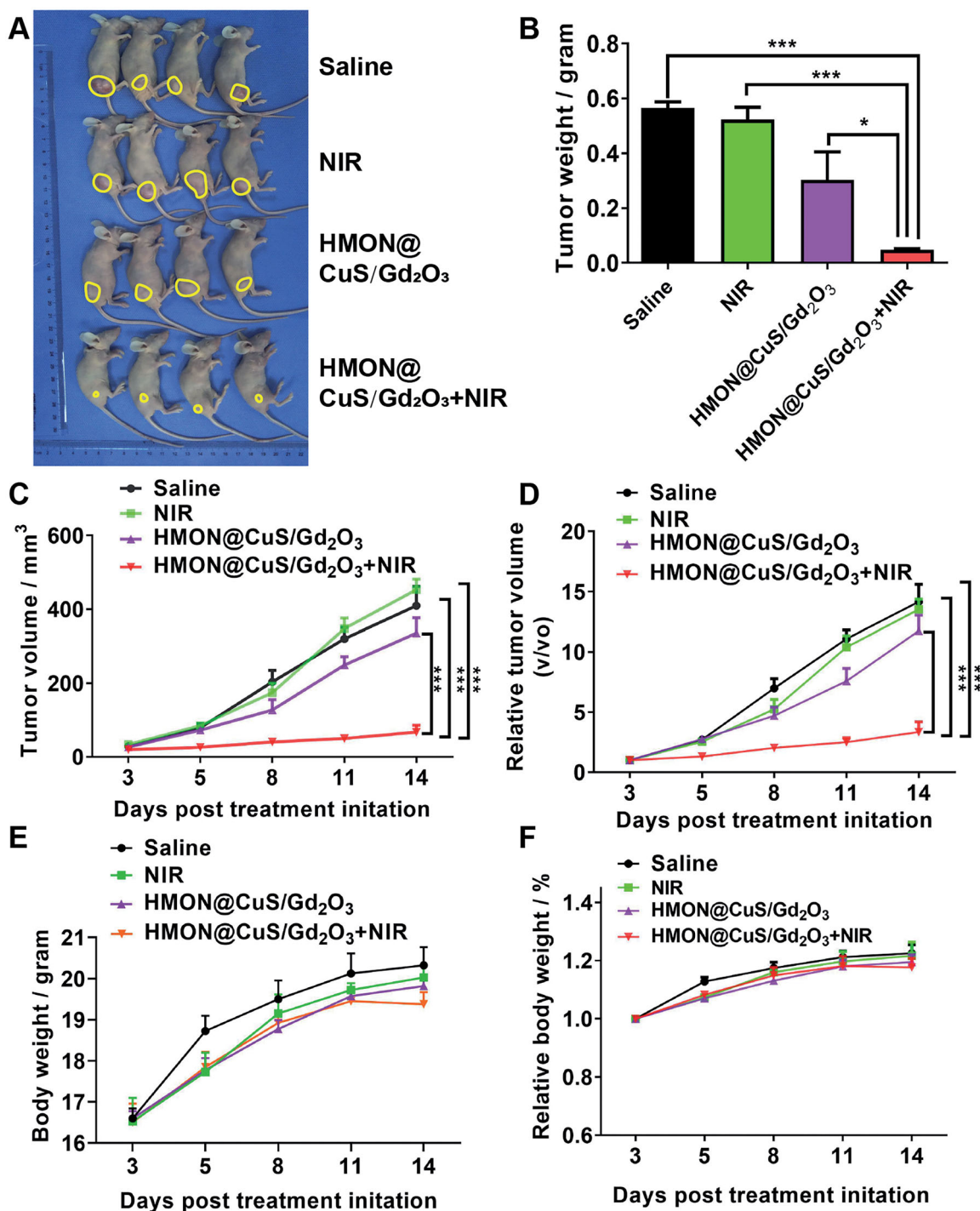
Figure 7. *In vivo* antitumour effects. (A) Images of tumors derived from mice after treatment with saline, saline plus NIR, HMON@CuS/Gd₂O₃, and HMON@CuS/Gd₂O₃ plus NIR. (B) Tumor weight of tumors derived from mice. (C&D) Tumor volume and relative tumor volume of tumors derived from mice. (D&E) Body weight and relative body weight of tumors derived from mice. $N = 4$, $*p < .05$, $***p < .001$.

lung, kidney, brain, and tumor tissues were further investigated, and the fluorescence intensity of tumor tissue was significantly higher than that of other tissues (Figure 6(B)). These results suggested that HMON@CuS/Gd₂O₃ NPs mainly accumulate in tumor tissue and reach a peak at 24 h; therefore, 24 h postinjection was an optimal therapeutic time window for therapy treatment *in vivo*. Fluorescence signals in the lung, spleen, liver, and kidney were also observed in the mice, indicating that the constructed NPs based on HMONs

undergo reticuloendothelial system uptake and renal excretion. The biocompatibility of NPs based on HMONs was tested in our earlier reported studies (Guo et al., 2020).

Subsequently, the IRT imaging abilities of HMON@CuS/Gd₂O₃ were further investigated in SKOV-3 tumor-bearing mice to evaluate the hyperthermia efficacy *in vivo*. The temperature of the tumor site was evaluated before intravenous tail injection of NPs and 24 h postinjection. The minimal tumor temperature only increased by approximately 2 °C

under NIR laser irradiation (.5 W/cm^2; 8 min) before injection. Although the minimal tumor temperature rose approximately 8 °C 24 h postinjection, the temperature rose rapidly to 42 °C within 180 s and was maintained at 43–445 °C in the following 300 s. These results indicated that HMON@CuS/Gd$_2$O$_3$ exhibits a mild PTT effect and good photothermal stability under NIR irradiation (.5 W/cm^2), a feature that may be much more attractive for clinical phototherapeutic treatment.

Furthermore, the *in vivo* T1-weighted MR imaging capacity of HMON@CuS/Gd$_2$O$_3$ was evaluated in SKOV-3 tumor-bearing mice using a 3.0 T Philips Ingenia MRI scanner. The intensity of the T1-weighted MR signal at the tumor site significantly increased 24 h after intravenous administration, and the signal-to-noise ratio (SNR) of the tumor 24 h after injection was 1.5 times higher than that before injection, validating the potential of HMON@CuS/Gd$_2$O$_3$ for T1-weighted MR imaging. These results consistently confirmed the tumor targeting capacity of HMON@CuS/Gd$_2$O$_3$.

Hence, the verified fluorescence, IRT, and MR imaging functionalities of HMON@CuS/Gd$_2$O$_3$ NPs synergistically provide various imaging features for precise cancer diagnostics and treatment. This multifunctional nanoplatform integrates the characteristics of high sensitivity, deep penetration and real-time navigation of fluorescence imaging, high spatial resolution, anatomical resolution, and good soft tissue resolution of MR imaging, as well as the tumor ablation characteristics of IRT.

In vivo antitumour of HMON@CuS/Gd$_2$O$_3$

To further analyze the *in vivo* antitumour potency, tumor-bearing mice were randomly divided into four groups: saline (negative control), saline under NIR irradiation (.5 W/cm^2; 8 min), HMON@CuS/Gd$_2$O$_3$, and HMON@CuS/Gd$_2$O$_3$ under NIR irradiation. The tumor suppression efficacy was quantitatively estimated by measuring the tumor size and tumor weight ((Figure 7). The mice in the saline group and saline under NIR irradiation group showed rapid tumor growth (almost 15-fold increase in the tumor volume on the 14th day), indicating that NIR irradiation alone does not play an antitumour role. The mice in the HMON@CuS/Gd$_2$O$_3$ group without NIR irradiation showed a similar tumor growth rate to those in the saline group, verifying that HMON@CuS/Gd$_2$O$_3$ alone has very limited antitumour efficacy. Interestingly, the tumor-bearing mice in the HMON@CuS/Gd$_2$O$_3$ under NIR irradiation group exhibited a marked tumor inhibition effect, and the tumor growth inhibition rate was approximately 80% compared with that in the control group. Additionally, no significant differences were observed in the body weight among these four groups, indicating that those treatments were well tolerated by the mice. Taken together, the results revealed that the photothermal therapy induced by HMON@CuS/Gd$_2$O$_3$ plus NIR irradiation efficiently kills tumor cells with fewer side effects, demonstrating that HMON@CuS/Gd$_2$O$_3$ NPs have promising applications for ovarian cancer treatment.

Conclusion

In summary, a new nanoplatform for endolysosomal escape and multimodal imaging was successfully constructed. The as-prepared NPs exhibit mild-temperature photothermal therapeutic effects under mild NIR irradiation (.5 W/cm^2), followed by lysosome vacuolation, disruption of lysosomal membrane integrity, and finally inhibition of the cell proliferation ability of ovarian cancer. Additionally, HMON@CuS/Gd$_2$O$_3$ have enhanced T1 MR imaging, FL imaging, and IRT imaging capacities, which can realize multimodal imaging-guided precision phototherapy. Taken together, the findings suggest that these well-synthesized nanoplatforms are promising anticancer agents to treat ovarian cancer and show great potential for biomedical applications.

Author contributions

Conceptualization, PFL, CLC, ZZG and PingL; methodology, PFL, BQL, AZC, and PanL; formal analysis, PFL, BQL, AZC, PanL and WLL; investigation, X.X. PFL, BQL, AZC, PanL and WLL; data curation, PFL, BQL, AZC, PanL and WLL; writing—original draft preparation, PFL, BQL, AZC, and PanL; writing—review and editing, all authors; supervision, CLC, ZZG and PingL; project administration, CLC; funding acquisition, CLC, and PFL. All authors have read and agreed to the published version of the manuscript.

Disclosure statement

No potential conflict of interest was reported by the author(s).

Institutional Review Board Statement

The study was approved by the Institutional Animal Care and Use Committee of the Nanfang Hospital, Southern Medical University.

Data availability statement

The data of this study are available from the corresponding author upon reasonable request.

References

Bray F, Ferlay J, Soerjomataram I, et al. (2018). Global cancer statistics 2018: GLOBOCAN estimates of incidence and mortality worldwide for 36 cancers in 185 countries. CA Cancer J Clin 68:394–424.

Chen G, Ke Z, Xu M, et al. (2012). Autophagy is a protective response to ethanol neurotoxicity. Autophagy 8:1577–89.

Chen L, Meng X, Liu M, et al. (2020). Biodegradable mesoporous organo-silica nanosheets for chemotherapy/mild thermotherapy of cancer: fast internalization, high cellular uptake, and high drug loading. ACS Appl Mater Interfaces 12:30234–46.

Chen Z, Liang Y, Feng X, et al. (2021). Vitamin-B12-conjugated PLGA-PEG nanoparticles incorporating miR-532-3p induce mitochondrial damage by targeting apoptosis repressor with caspase recruitment domain (ARC) on CD320-overexpressed gastric cancer. Mater Sci Eng C Mater Biol Appl 120:111722.

Fang J, Chandrasekharan P, Liu XL, et al. (2014). Manipulating the surface coating of ultra-small Gd2O3 nanoparticles for improved T1-weighted MR imaging. Biomaterials 35:1636–42.

Guo W, Chen Z, Chen J, et al. (2020). Biodegradable hollow mesoporous organosilica nanotheranostics (HMON) for multi-mode imaging and mild photo-therapeutic-induced mitochondrial damage on gastric cancer. J Nanobiotechnology 18:99.

Guo W, Chen Z, Feng X, et al. (2021). Graphene oxide (GO)-based nano-sheets with combined chemo/photothermal/photodynamic therapy to overcome gastric cancer (GC) paclitaxel resistance by reducing mito-chondria-derived adenosine-triphosphate (ATP). J Nanobiotechnology 19:146.

Guo W, Deng L, Yu J, et al. (2018). Sericin nanomicelles with enhanced cellular uptake and pH-triggered release of doxorubicin reverse can-cer drug resistance. Drug Deliv 25:1103–16.

Hadipour Moghaddam SP, Yazdimamaghani M, Ghandehari H. (2018). Glutathione-sensitive hollow mesoporous silica nanoparticles for con-trolled drug delivery. J Control Release 282:62–75.

He J, Ai L, Liu X, et al. (2018). Plasmonic CuS nanodisk assembly based composite nanocapsules for NIR-laser-driven synergistic chemo-photo-thermal cancer therapy. J Mater Chem B 6:1035–43.

Huang P, Chen Y, Lin H, et al. (2017). Molecularly organic/inorganic hybrid hollow mesoporous organosilica nanocapsules with tumor-spe-cific biodegradability and enhanced chemotherapeutic functionality. Biomaterials 125:23–37.

Jayson GC, Kohn EC, Kitchener HC, Ledermann JA. (2014). Ledermann J A. Ovarian cancer. Lancet (London, England) 384:1376–88.

Jiang H, Guo Y, Wei C, et al. (2021). Nanocatalytic innate immunity acti-vation by mitochondrial DNA oxidative damage for tumor-specific therapy. Adv Mater 33:e2008065.

Jiang S, Xiao M, Sun W, et al. (2020). Synergistic anticancer therapy by ovalbumin encapsulation-enabled tandem reactive oxygen species generation. Angew Chem Int Ed Engl 59:20008–16.

Jin C, Li G, Wu X, et al. (2021). Robust packing of a self-assembling irid-ium complex via endocytic trafficking for long-term lysosome track-ing. Angew Chem Int Ed Engl 60:7597–601.

Lheureux S, Gourley C, Vergote I, Oza AM. (2019). Epithelial ovarian can-cer. Lancet 393:1240–53.

Li K, Lin C, He Y, et al. (2020). Engineering of cascade-responsive nano-platform to inhibit lactate efflux for enhanced tumor chemo-immuno-therapy. ACS Nano 14:14164–80.

Li L, Yang Z, Fan W, et al. (2020). In situ polymerized hollow mesoporous organosilica biocatalysis nanoreactor for enhancing ROS-mediated anticancer therapy. Adv Funct Mater 30:1907716.

Li N, Sun Q, Yu Z, et al. (2018). Nuclear-targeted photothermal therapy prevents cancer recurrence with near-infrared triggered copper sul-fide nanoparticles. ACS Nano 12:5197–206.

Liu H, Du Y, St-Pierre JP, et al. (2020). Bioenergetic-active materials enhance tissue regeneration by modulating cellular metabolic state. Sci Adv 6:eaay7608.

Mukherjee AB, Appu AP, Sadhukhan T, et al. (2019). Emerging new roles of the lysosome and neuronal ceroid lipofuscinoses. Mol Neurodegener 14:4.

Nakamura T, Fahmi M, Tanaka J, et al. (2019). Genome-wide analysis of whole human glycoside hydrolases by data-driven analysis in silico. IJMS 20:6290.

Park SJ, Park JY, Yang HK, et al. (2018). Biocompatible sphere, square prism and hexagonal rod Gd2O3:Eu3+@SiO2 nanoparticles: the effect of morphology on multi-modal imaging. Colloids Surf B Biointerfaces 172:224–32.

Qu F, Wang P, Zhang K, et al. (2020). Manipulation of mitophagy by "all-in-one" nanosensitizer augments sonodynamic glioma therapy. Autophagy 16:1413–35.

Shi L, Wu W, Duan Y, et al. (2020). Light-induced self-escape of spherical nucleic acid from endo/lysosome for efficient non-cationic gene deliv-ery. Angew Chem Int Ed Engl 59:19168–74.

Sung H, Ferlay J, Siegel RL, et al. (2021). Global cancer statistics 2020: GLOBOCAN estimates of incidence and mortality worldwide for 36 cancers in 185 countries. CA 71:209–49.

Tang HX, Liu CG, Zhang JT, et al. (2020). Biodegradable quantum compo-sites for synergistic photothermal therapy and copper-enhanced chemotherapy. ACS Appl Mater Interfaces 12:47289–98.

Wu J, Meng Z, Exner AA, et al. (2021). Biodegradable cascade nanocata-lysts enable tumor-microenvironment remodeling for controllable CO release and targeted/synergistic cancer nanotherapy. Biomaterials 276:121001.

Yu Q, Tang X, Zhao W, et al. (2021). Mild hyperthermia promotes immune checkpoint blockade-based immunotherapy against meta-static pancreatic cancer using size-adjustable nanoparticles(★). Acta Biomater 133:244–56.

Zhang L, Sun Y, Fei M, et al. (2014). Disruption of chaperone-mediated autophagy-dependent degradation of MEF2A by oxidative stress-induced lysosome destabilization. Autophagy 10:1015–35.

Zhang P, Zhang Y, Ding X, et al. (2020). A multistage cooperative nano-platform enables intracellular co-delivery of proteins and chemothera-peutics for cancer therapy. Adv Mater 32:e2000013.

Zhang Y, Li Y, Ma J, et al. (2018). Convenient preparation of charge-adaptive chitosan nanomedicines for extended blood circulation and accelerated endosomal escape. Nano Res 11:4278–92.

Zhu H, Li Q, Liao T, et al. (2021). Metabolomic profiling of single enlarged lysosomes. Nat Methods 18:788–98.

Zhu L, Jorgensen JR, Li M, et al. (2017). ESCRTs function directly on the lysosome membrane to downregulate ubiquitinated lysosomal mem-brane proteins. eLife 6:e26403.

Zohdiaghdam R, Riyahi-Alam N, Moghimi HR, et al. (2013). Development of a novel lipidic nanoparticle probe using liposomal encapsulated Gd$_2$O$_3$-DEG for molecular MRI. J Microencapsul 30:613–23.